

Nonmodal Growth of Traveling Waves on Blunt Cones at Hypersonic Speeds

Pedro Paredes,^{*}

National Institute of Aerospace, Hampton, VA 23666, USA

Meelan M. Choudhari,[†] Fei Li,[‡]

NASA Langley Research Center, Hampton, VA 23681, USA

Joseph S. Jewell,[§] Roger L. Kimmel[¶]

U.S. Air Force Research Laboratory, Wright-Patterson Air Force Base, OH 45433, USA

The existing database of transition measurements in hypersonic ground facilities has established that, as the nosetip bluntness is increased, the onset of boundary layer transition over a circular cone at zero angle of attack shifts downstream. However, this trend is reversed at sufficiently large values of the nose Reynolds number, so that the transition onset location eventually moves upstream with a further increase in nose-tip bluntness. Because modal amplification is too weak to initiate transition at moderate-to-large bluntness values, nonmodal growth has been investigated as the potential basis for a physics-based model for the frustum transition. The present analysis investigates the nonmodal growth of traveling disturbances initiated within the nose-tip vicinity that peak within the entropy layer. Results show that, with increasing nose bluntness, both planar and oblique traveling disturbances experience appreciable energy amplification up to successively higher frequencies. For moderately blunt cones, the initial nonmodal growth is followed by a partial decay that is more than overcome by an eventual, modal growth as Mack-mode waves. For larger bluntness values, the Mack-mode waves are not amplified anywhere upstream of the experimentally measured transition location, but the traveling modes still undergo a significant amount of nonmodal growth. This finding does not provide a definitive link between optimal growth and the onset of transition, but it is qualitatively consistent with the experimental observations that frustum transition in the absence of sufficient Mack-mode amplification implies a double peak in disturbance amplification and the appearance of transitional events above the boundary-layer edge.

Nomenclature

E	=	total energy norm
F	=	disturbance frequency [s^{-1}]
G	=	energy gain
h_t	=	total enthalpy [$m^2 s^{-2}$]
h_ξ	=	streamwise metric factor
h_ζ	=	spanwise metric factor [m]
J	=	objective function
L	=	reference length [m]
m	=	azimuthal wavenumber [rad^{-1}]
M	=	Mach number
N	=	Logarithmic amplification factor
$\hat{\mathbf{q}}$	=	vector of amplitude variables

^{*}Research Engineer, Computational AeroSciences Branch, NASA LaRC. AIAA Senior Member

[†]Research Scientist, Computational AeroSciences Branch. AIAA Associate Fellow

[‡]Research Scientist, Computational AeroSciences Branch.

[§]Research Scientist, (Spectral Energies, LLC), AFRL/RQHF. AIAA Senior Member

[¶]Principal Aerospace Engineer, AFRL/RQHF. AIAA Associate Fellow

$\check{\mathbf{q}}$	=	vector of disturbance function variables
$\bar{\mathbf{q}}$	=	vector of base flow variables
$\tilde{\mathbf{q}}$	=	vector of perturbation variables
Re_∞	=	freestream unit Reynolds number [m^{-1}]
Re_{R_N}	=	Reynolds number based on nose radius
r_b	=	local radius of axisymmetric body at the axial station of interest [m]
R_N	=	nose radius [m]
T	=	temperature [K]
T_w	=	wall temperature [K]
$T_{w,ad}$	=	adiabatic wall temperature [K]
(u, v, w)	=	streamwise, wall-normal, and azimuthal velocity components [m s^{-1}]
(x, y, z)	=	Cartesian coordinates
α	=	streamwise wavenumber [m^{-1}]
δ_h	=	boundary-layer thickness [m]
δ_S	=	entropy-layer thickness [m]
κ	=	streamwise curvature [m^{-1}]
ω	=	disturbance angular frequency [s^{-1}]
ρ	=	density [kg m^{-3}]
(ξ, η, ζ)	=	streamwise, wall-normal, and azimuthal coordinates
$\Delta\xi$	=	streamwise interval considered for optimal growth analysis [m]
ΔS	=	entropy increment [$\text{kg m}^2 \text{s}^{-2} \text{K}^{-1}$]
θ	=	cone half-angle [$^\circ$]
\mathbf{M}	=	energy weight matrix
Superscripts		
*	=	dimensional value
H	=	conjugate transpose
Subscript		
∞	=	freestream value
0	=	initial position
1	=	final position
T	=	transition location
Abbreviations		
AFRL	=	Air Force Research Laboratory
DNS	=	direct numerical simulation
DPLR	=	data parallel-line relaxation
HLNSE	=	harmonic, linearized Navier-Stokes equations
NS	=	Navier-Stokes
LIF	=	laser-induced fluorescence
PNS	=	parabolic Navier-Stokes equations
PSE	=	parabolized stability equations
RHLNSE	=	reduced form of the harmonic, linearized Navier-Stokes equations

I. Introduction

Laminar-turbulent transition of boundary-layer flows can have a strong impact on the performance of hypersonic vehicles because of its influence on the surface skin friction and aerodynamic heating. Therefore, the prediction and control of transition onset and the associated variation in aerothermodynamic parameters in high-speed flows is a key issue for optimizing the performance of the next-generation aerospace vehicles. Although many practical aerospace vehicles have blunt, hemispherical and ogival nose-tips, the mechanisms that lead to boundary-layer instability and transition on such geometries are not well understood as yet. A detailed review of boundary layer transition over sharp and blunt cones in a hypersonic freestream is given by Schneider [1]. As described therein, both experimental and numerical studies have shown that the modal growth of Mack-mode instabilities (or, equivalently, the so-called second-mode waves) is responsible for laminar-turbulent transition on sharp, axisymmetric cones at zero angle of attack. Studies have also shown that an increased nose-tip bluntness, i.e., a larger radius of hemispherical or ogival nose-tips,

leads to the formation of an entropy layer that may extend well beyond the vicinity of the nose-tip region [2]. The entropy layer has been shown to have a stabilizing effect on the amplification of Mack-mode instabilities, consistent with the experimental observation that the onset of transition is displaced downstream as the nose bluntness is increased. However, while the boundary layer flow continues to become more stable with an increasing nose bluntness according to linear modal stability analysis, experiments indicate that the downstream movement in transition actually slows down and eventually reverses as the nose bluntness exceeds a certain critical range of values. The observed trend in transition onset at moderate to large values of nose bluntness is contrary to the predictions of linear stability theory, and therefore, it must be explained using a different paradigm. Even though no satisfactory theory has been proposed as yet to explain the phenomenon of transition reversal, the latter is believed to be somehow related to external forcing in the form of either surface roughness and/or freestream turbulence. Given the absence of modal instability as an underlying cause, nonmodal disturbance amplification induced by the external forcing has been proposed as the basis of a physics-based model for the transition reversal phenomenon [3–5].

A recent collaborative effort under the NATO STO group AVT-240 on Hypersonic Boundary-Layer Transition Prediction focused on the problem of transition over axisymmetric cones with blunt, hemispherical nose-tips and on the potential role of transient growth in the transition reversal phenomenon [3, 5]. Figure 1 shows the comparison of wind tunnel measurements in both U.S. and European facilities at freestream Mach numbers from 6 to 12. All of the datasets display two distinct regions, viz., a “small bluntness” wherein the transition location moves downstream with increased bluntness, and a “large bluntness” region wherein the transition location rapidly moves upstream. The nose Reynolds number separating these two regions, i.e., where the transition reversal begins, appears to vary across the different datasets. Experiments have suggested that, following the onset of transition reversal, the transition process is influenced by (uncontrolled) disturbances due to the nose-tip roughness.

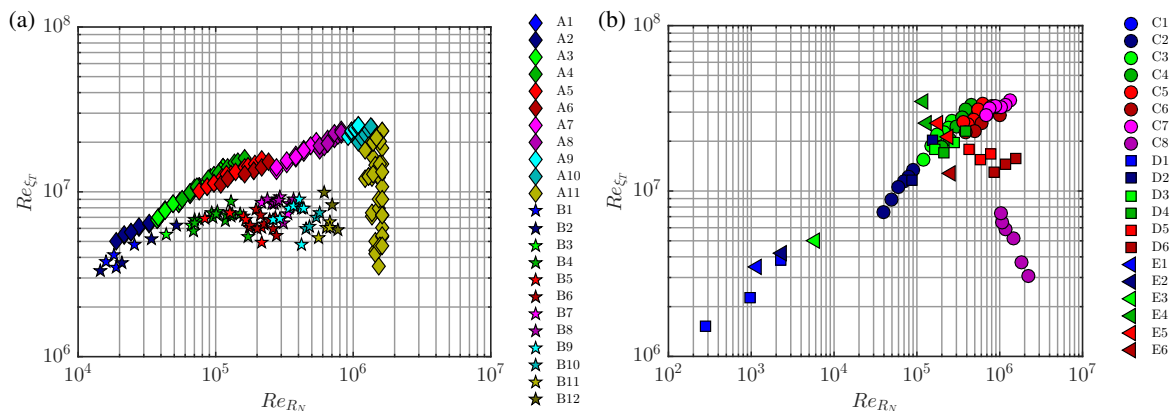


Fig. 1 Transition Reynolds number based on freestream as a function of the nose Reynolds number at (a) Mach 6 and (b) Mach 9 to 10, which illustrates the effect of bluntness and the transition reversal. The letter of the legend refers to the experimental datasets; namely, (A) and (C) [2], (B) [6], (D) [7], and (E) [8, 9]. The numbers denote different nose-tip radius. Extracted from Ref. [5].

In contrast to Stetson’s blunt cone experiments, which measured just the transition location, Marineau et al. [7] also measured the boundary-layer instabilities in Tunnel 9 at Mach 10 and freestream unit Reynolds number of $17 \times 10^6 \text{ m}^{-1}$ on 7° half-angle cones by using a large number of high-frequency response pressure sensors (PCB®-132). These measurements captured the evolution of the pressure fluctuations over the surface of the cone. For the 12.7 mm nosetip ($Re_{RN} = 215900$), the start of transition occurs prior to significant growth of the second mode. However, Marineau et al. [7] reported high spectral amplitudes near the nosetip across the entire frequency range of measurements up to 850 kHz, and a transient decrease in the downstream region, eventually followed by an increase due to the appearance of second-mode instabilities. The initial peak was assumed to be related to the entropy layer. Furthermore, the laser-induced-fluorescence (LIF) based schlieren measurements from Grossir et al. [10] on a blunt 7-degree half-angle cone at Mach 11.9 in the Von Kármán Institute Longshot hypersonic wind tunnel revealed disturbances with a rather different structure than the usual rope waves associated with second mode disturbances. For example, disturbances that extend above the edge of the boundary layer are seen in Fig. 2, which shows measurements above a cone with 4.75 mm nose-tip radius. These disturbances were not present in the schlieren images obtained for sharper cones. Finally, Zanchetta [11] has reported time-resolved heat transfer measurements on a 5-degree half-angle cone at Mach 9 in the

Imperial College Gun Tunnel. Their data indicate that, after transition reversal has occurred, the transitional events originate inside the near-nose region and subsequently convect downstream. The frequency of these events was linked to the severity of the roughness environment. Their investigation into roughness effects within the transition reversal regime [11] has revealed that two-dimensional annular trips are likely to be more effective in enhancing transition than three-dimensional roughness.

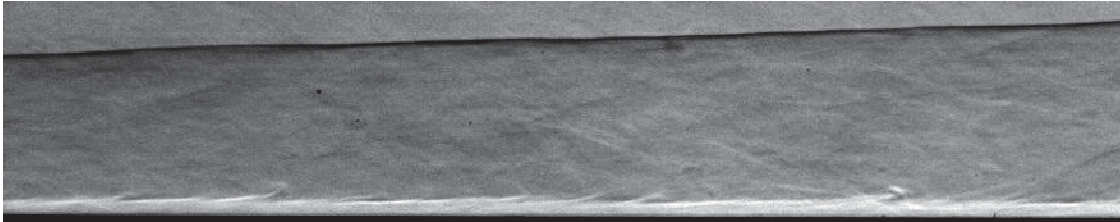


Fig. 2 LIF-based schlieren flow visualization on 4.75 mm radius nose-tip 7-degree half-angle cone in the VKI Longshot hypersonic wind tunnel at $M_\infty = 11.9$ and $Re_\infty = 11.6 \times 10^6 \text{ m}^{-1}$. Field of view extends from $x = 625$ mm until the end of the cone at 806 mm. Disturbances extending past the boundary-layer thickness are visible. Extracted from Ref. [5].

The available linear stability analyses [7, 12–16] agree that transition reversal cannot be predicted by considering just modal instability amplification, because Mack’s second mode is strongly stabilized by the presence of the entropy layer and the first mode, commonly responsible for the onset on transition at supersonic boundary-layer-edge conditions, is not destabilized. Additionally, the modal amplification of entropy-layer modes is marginal as reported by Refs. [17, 18]. Because of the failure of the modal instability theory in predicting transition upstream of the swallowing location of the entropy layer, Paredes et al. [3] proposed using nonmodal growth as the basis of a physics-based model for the experimentally observed onset of transition. Their results indicate that stationary disturbances that are initiated within the nose-tip vicinity can undergo appreciable nonmodal amplification that increases with the nose-tip bluntness. This finding does not provide a definite link between transient growth and the onset of transition, but it is qualitatively consistent with the experimental observations that frustum transition during the reversal regime was highly sensitive to wall roughness, and furthermore, was dominated by disturbances originating near the nose-tip. The predictions for optimal transient growth were used to design an azimuthally periodic array of microroughness elements located near the sonic point at the nose-tip [3]. The measurements showed that variable bluntness models with similar values of roughness Reynolds number, Re_{kk} , affected transition only on the blunter cone, demonstrating that transition onset in this case is associated with the combined effects of nose bluntness and surface roughness. Computations by Cook et al. [4], Paredes et al. [5] have identified certain planar traveling disturbances that may peak within the entropy layer and, furthermore, are able sustain a significant amount of nonmodal amplification. As a result of this amplification, these nonstationary disturbances could also play a role in the transition reversal phenomenon if they can be excited under a natural disturbance environment.

The present paper continues the study of Paredes et al. [5] related to the growth of disturbances that may lead to laminar-turbulent transition upstream of the swallowing location of the entropy layer. The specific focus of this paper corresponds to a variable bluntness, 7-degree cone that was tested in the AFRL Mach-6 high-Reynolds-number facility [16]. The methodology used to investigate the nonmodal amplification of disturbances is summarized in Section II. Next, the laminar boundary layer flow over the selected configurations and results for the modal and nonmodal growth of traveling disturbances are presented in Section III. The summary and concluding remarks are presented in Section IV.

II. Theory

In this section, we outline the methodology used for the analysis of disturbance amplification over the blunt cone configurations of interest. Following the work of Ref. [5], we use the harmonic linearized Navier Stokes equations (HLNSE), the reduced form of the HLNSE (RHLNSE), and the linear parabolized stability equations (PSE) frameworks to investigate both modal and nonmodal disturbances. Optimal growth analysis of stationary disturbances within the PSE framework [19–23] bears strong similarities with the optimization approach based on the linearized boundary-region equations [24–26]. As explained below, the PSE approach can also be extended to the unsteady disturbances examined in this paper [5].

A. Governing Equations for Modal and Nonmodal Disturbances

The present work is focused on the boundary layers over axisymmetric bodies in a hypersonic flow. The freestream conditions and geometries are selected to match selected configurations from the AFRL experiments [16] with variable bluntness, 7-degree half-angle cones. For this problem, the computational coordinates are defined as an orthogonal, body-fitted coordinate system, with (ξ, η, ζ) denoting the streamwise, wall-normal, and azimuthal coordinates, respectively, and (u, v, w) representing the corresponding velocity components. Density and temperature are denoted by ρ and T . The metric factors are defined as

$$h_\xi = 1 + \kappa\eta, \quad (1)$$

$$h_\zeta = r_b + \eta \cos(\theta), \quad (2)$$

where h_ξ and h_ζ are associated with the streamwise and azimuthal curvature, respectively, κ denotes the streamwise curvature, r_b is the local radius, and θ is the local half-angle along the axisymmetric surface, i.e., $\sin(\theta) = dr_b/d\xi$.

Linear perturbations that are assumed to be harmonic in both time and the azimuthal coordinate can be written as

$$\tilde{\mathbf{q}}(\xi, \eta, \zeta, t) = \check{\mathbf{q}}(\xi, \eta) \exp [i(m\zeta - \omega t)] + c.c., \quad (3)$$

where c.c. denotes complex conjugate. The streamwise and azimuthal wavenumbers are α and m , respectively; and ω is the angular frequency of the perturbation. The Cartesian coordinates are represented by (x, y, z) . The vector of perturbation variables is denoted by $\tilde{\mathbf{q}}(\xi, \eta, \zeta, t) = (\tilde{\rho}, \tilde{u}, \tilde{v}, \tilde{w}, \tilde{T})^T$ and the vector of disturbance functions is $\check{\mathbf{q}}(\xi, \eta) = (\check{\rho}, \check{u}, \check{v}, \check{w}, \check{T})^T$. The vector of basic state variables is $\hat{\mathbf{q}}(\xi, \eta) = (\hat{\rho}, \hat{u}, \hat{v}, \hat{w}, \hat{T})^T$. The disturbance functions $\check{\mathbf{q}}(\xi, \eta)$ satisfy the harmonic form of linearized Navier-Stokes equations (HLNSE),

$$\mathbf{L}_{HLNSE} \check{\mathbf{q}}(\xi, \eta) = \left(\mathbf{A} + \mathbf{B} \frac{\partial}{\partial \eta} + \mathbf{C} \frac{\partial^2}{\partial \eta^2} + \mathbf{D} \frac{1}{h_\xi} \frac{\partial}{\partial \xi} + \mathbf{E} \frac{1}{h_\xi} \frac{\partial^2}{\partial \xi \partial \eta} + \mathbf{F} \frac{1}{h_\xi^2} \frac{\partial^2}{\partial \xi^2} \right) \check{\mathbf{q}}(\xi, \eta) = 0. \quad (4)$$

The linear operators \mathbf{A} , \mathbf{B} , \mathbf{C} , \mathbf{D} , \mathbf{E} , \mathbf{F} depend on the basic state variables and parameters, and on the angular frequency, streamwise wavenumber, and azimuthal wavenumber of the perturbation.

The PSE approximation to the HLNSE is based on isolating the rapid phase variations in the streamwise direction via the disturbance ansatz

$$\check{\mathbf{q}}(\xi, \eta) = \hat{\mathbf{q}}(\xi, \eta) \exp \left[i \int_{\xi_0}^{\xi} \alpha(\xi') d\xi' \right], \quad (5)$$

where the unknown, streamwise varying wavenumber $\alpha(\xi)$ is determined in the course of the solution by imposing an additional constraint

$$\int_{\eta} \hat{\mathbf{q}}^* \frac{\partial \hat{\mathbf{q}}}{\partial \xi} h_\xi h_\zeta d\eta = 0, \quad (6)$$

where the amplitude functions $\hat{\mathbf{q}}(\xi, \eta) = (\hat{\rho}, \hat{u}, \hat{v}, \hat{w}, \hat{T})^T$ vary slowly in the streamwise direction in comparison with the phase term $\exp \left[i \int_{\xi_0}^{\xi} \alpha(\xi') d\xi' \right]$. Substituting Eq. (5) into Eq. (4) and invoking scale separation between the streamwise coordinate and the other two directions to neglect the viscous terms with streamwise derivatives, one obtains the PSE in the form

$$\mathbf{L}_{PSE} \hat{\mathbf{q}}(\xi, \eta) = \left(\mathbf{A} + \mathbf{B} \frac{\partial}{\partial \eta} + \mathbf{C} \frac{\partial^2}{\partial \eta^2} + \mathbf{D} \frac{1}{h_1} \frac{\partial}{\partial \xi} \right) \hat{\mathbf{q}}(\xi, \eta) = 0. \quad (7)$$

As discussed in Ref. [5], Eq. (6) constrains the PSE disturbances to have a unique, local wavenumber at any streamwise location and, therefore, the PSE are likely to encounter difficulties when the perturbation field includes multiple disturbances with disparate variation along the streamwise direction. Optimal growth perturbations are known to include a superposition of multiple eigenmodes of the quasiparallel disturbance equations, and therefore, additional simplifications must accrue in applying the PSE for optimal growth predictions. To confirm the validity of the PSE approximation, Paredes et al. [5] proposed using the reduced form of HLNSE, referred to as RHLNSE, which omits just the second order, viscous derivative terms in ξ from the linearized Navier-Stokes equations in Eq. (4). This simplification is consistent when the streamwise disturbance wavelength is much larger than the thickness of the mean boundary layer. Thus, after neglecting the second derivative terms in ξ , one obtains the RHLNSE:

$$\mathbf{L}_{RHLNSE} \check{\mathbf{q}}(\xi, \eta) = \left(\mathbf{A} + \mathbf{B} \frac{\partial}{\partial \eta} + \mathbf{C} \frac{\partial^2}{\partial \eta^2} + \mathbf{D} \frac{1}{h_\xi} \frac{\partial}{\partial \xi} + \mathbf{E} \frac{1}{h_\xi} \frac{\partial^2}{\partial \xi \partial \eta} \right) \check{\mathbf{q}}(\xi, \eta) = 0. \quad (8)$$

The PSE (7) and RHLNSE (8) retain some streamwise ellipticity via the streamwise pressure gradient term,

$$\frac{\partial \bar{p}}{\partial \xi} = i\alpha \hat{p} + \frac{\partial \hat{p}}{\partial \xi}, \quad (9)$$

in the streamwise momentum equation [27–30] and, hence, a marching solution would not be feasible in all cases. However, our computations revealed that it was feasible to obtain marching solutions to these equations for the flow conditions of interest. For purely stationary disturbances ($\omega = 0$ and $\alpha = 0$), the streamwise pressure gradient term can be dropped from the equations as justified in Refs. [20, 31]. For nonstationary perturbations ($\omega \neq 0$), a commonly adopted solution is to replace $\partial \hat{p} / \partial \xi$ by $\Omega_{PNS} \partial \hat{p} / \partial \xi$, where Ω_{PNS} is the Vigneron parameter [32–34]. This parameter was originally introduced for the integration of the parabolized Navier-Stokes (PNS) equations, and is determined by

$$\Omega_{PNS} = \min(1, M_\xi^2), \quad (10)$$

where M_ξ is the local streamwise Mach number. The Vigneron approximation ensures numerical stability of the marching scheme by suppressing upstream influence within the solution. For locally supersonic flow, the equations are not altered because $\Omega_{PNS} = 1$. For a disturbance field with $\alpha \neq 0$, a portion of the elliptic behavior is absorbed in the wave part via the term $i\alpha \hat{p}$ and the residual upstream influence can be suppressed by choosing a sufficiently large marching step [29], without having to invoke the Vigneron approximation. The streamwise evolution of optimal disturbances obtained using Eq. (10) can be verified a posteriori using the PSE (7) as well as the full set of linearized disturbance equations (4).

B. Optimal Growth Theory

The optimal initial disturbance, $\tilde{\mathbf{q}}_0$, is defined as the initial (i.e., inflow) condition at ξ_0 that maximizes the objective function, J , which is defined as a measure of disturbance growth over a specified interval $[\xi_0, \xi_1]$. The definition used in the present study correspond to the outlet energy gain $J = G^{out}$ that is defined as

$$G^{out} = \frac{E(\xi_1)}{E(\xi_0)}, \quad (11)$$

where E denotes the energy norm of $\tilde{\mathbf{q}}$. The energy norm is defined as

$$E(\xi) = \int_{\eta} \hat{\mathbf{q}}(\xi, \eta)^H \mathbf{M}_E \hat{\mathbf{q}}(\xi, \eta) h_\xi h_\zeta d\eta, \quad (12)$$

where \mathbf{M}_E is the energy weight matrix and the superscript H denotes conjugate transpose. The selection of $J = G^{out}$ corresponds to the ‘‘outlet energy gain’’ that is commonly used in studies of the optimal-perturbation problem [24, 25].

The choice of the energy norm is known to influence the optimal initial perturbation as well as the magnitude of energy amplification [21, 26, 35]. The positive-definite energy norm used here was derived by Chu [36] and used by Mack [37] and Hanifi et al. [38] for linear stability theory. This energy norm is defined as

$$\mathbf{M}_E = \text{diag} \left[\frac{\bar{T}(\xi, \eta)}{\gamma \bar{\rho}(\xi, \eta) M^2}, \bar{\rho}(\xi, \eta), \bar{\rho}(\xi, \eta), \bar{\rho}(\xi, \eta), \frac{\bar{\rho}(\xi, \eta)}{\gamma(\gamma - 1) \bar{T}(\xi, \eta) M^2} \right]. \quad (13)$$

In the present study, the disturbance amplification is also expressed in terms of the logarithmic amplification ratio, the so-called N -factor, based on the total energy norm, which is defined as

$$N_E = \frac{1}{2} \ln(G_E^{out}) = - \int_{\xi_0}^{\xi_1} \alpha_i(\xi') d\xi' + 1/2 \ln[\hat{E}(\xi_1)/\hat{E}(\xi_0)]. \quad (14)$$

Furthermore, the present study uses the N -factor based in other disturbance magnitude norms, as the kinetic energy, N_K . This definition is equivalent to that of Eq. (14), but with the kinetic energy norm defined as

$$\mathbf{M}_K = \text{diag} [0, \bar{\rho}(\xi, \eta), \bar{\rho}(\xi, \eta), \bar{\rho}(\xi, \eta), 0]. \quad (15)$$

The variational formulation of the problem to determine the maximum of the objective functional J leads to an optimality system [22], which is solved in an iterative manner, starting from a random solution at ξ_0 that must satisfy the boundary conditions. The HLNSE, RHLNSE, or PSE, $\mathbf{L}\tilde{\mathbf{q}} = 0$, are used to integrate $\tilde{\mathbf{q}}$ up to ξ_1 , where the final optimality condition is used to obtain the initial condition for the backward adjoint equations integration, $\mathbf{L}^\dagger \tilde{\mathbf{q}}^\dagger = 0$. At ξ_0 , the adjoint solution is used to calculate the new initial condition for the forward integration with the initial optimality condition. The iterative procedure finishes when the value of G has converged up to a certain tolerance, which was set to 10^{-4} in the present computations.

C. Discretization and Boundary Conditions

Stable high-order finite-difference schemes [39, 40] of sixth order are used for discretization of the stability equations on the nonuniform grid along the the wall-normal direction. For the results presented here, the wall-normal direction is discretized with $N_\eta = 201$, with the nodes being clustered toward the wall. The discretized PSE and RHLNSE are integrated along the streamwise coordinate by using second-order backward differentiation. The HLNSE are discretized along the streamwise coordinate with centered, fourth-order finite differences. The number of discretization points in both directions was varied in selected cases to ensure the numerical convergence of the results.

No-slip, isothermal boundary conditions are used at the wall, i.e., $\hat{u} = \hat{v} = \hat{w} = \hat{T} = 0$. The farfield boundary is set just below the shock layer and, unless indicated otherwise, the amplitude functions are forced to decay at the farfield boundary by imposing the Dirichlet conditions $\hat{\rho} = \hat{u} = \hat{v} = \hat{T} = 0$. Verification of the present optimal growth module against available transient growth results from the literature is described in Ref. [22].

III. Stability Analysis of Hypersonic Blunt Cones

This section presents modal and nonmodal growth analysis for blunt circular cones at selected flow conditions involving a subset of configurations from the experiments conducted by Stetson [2] and Jewell et al. [16] in the Air Force Research Laboratory (AFRL) Mach 6 High Reynolds Number facility. Modal instability analysis for the AFRL configurations has been already performed by Jewell and Kimmel [15]. Based on their results, both first-mode and Mack-mode waves were either damped or, at most, weakly unstable for the present configurations; and therefore, transition reversal cannot be predicted with the modal instability analysis as discussed previously. Another modal instability mechanism that might play a role in the transition reversal is the entropy-layer instability [17, 18]. However, although not shown, our analysis did not reveal any sufficiently amplified entropy-layer modes for the configurations of interest. Therefore, in the absence of modal growth, the transient growth mechanism is investigated as a potential cause for the onset of transition. First, the basic state solutions at the conditions of interest are presented in subsection III.A. Second, the modal and nonmodal growth characteristics of the selected blunt cones configurations are presented in subsections III.B and III.C, respectively.

A. Numerical Results

The basic states used in the present analysis correspond to the laminar boundary layer flow over the selected blunt cone configurations. The laminar boundary-layer flows were computed by [15] with reacting, axisymmetric Navier-Stokes equations on a structured grid. The solver was a version of the NASA data parallel-line relaxation (DPLR) code [41], that is included as part of the STABL-2D software suite, as described by Johnson [42] and Johnson et al. [43]. This flow solver employs a second-order-accurate finite-volume formulation. The inviscid fluxes are based on the modified Steger-Warming flux vector splitting method with a monotonic upstream-center scheme for the conservation laws (MUSCL) limiter. The time integration method is the implicit, first-order data parallel line relaxation (DPLR) method. The effects of chemistry and molecular vibration are negligible at the present flow conditions. Thus, the high enthalpy effects are omitted from the calculations. The viscosity is varied according to the Sutherland's law and the heat conductivity is calculated by using Eucken's relation. Additional details about the basic state solution and the grid convergence study are given by Jewell and Kimmel [15].

The AFRL Mach 6 facility operates at stagnation pressures p_0 from 700 to 2100 psi (4.83 to 14.5 MPa). The working fluid is air and is treated as an ideal gas because of the relatively low temperature and pressure. The blunt cones used in the experiments by Stetson [2] had a half-angle of 8° and a base radius of 2.0 in. (0.0508 m). A total of 196 experiments encompassing 108 unique conditions comprised the database obtained by Stetson [2] at Mach 6. The present analysis uses the 7° half-angle variable-bluntness cone that is currently used in the experiments in the AFRL Mach 6 facility by Jewell et al. [16]. The actual freestream Mach number is $M_\infty = 5.9$. The thermal wall condition is isothermal, with a constant wall temperature of $\bar{T}_w = 300.0$ K that corresponds to a wall-to-adiabatic temperature ratio of $\bar{T}_w/\bar{T}_{w,ad} = 0.57$. Table 1 shows the details of the configurations selected for the present study. The experimentally measured transition locations, ξ_T , by Jewell et al. [16] are included. The corresponding predictions for Mack-mode N -factors, i.e., $N_{MM}(\xi_T)$, together with the corresponding disturbance frequency, $F_{MM}(\xi_T)$, computed during the present study, are also shown in Table 1. For the baseline configuration of a nearly sharp cone with $R_N = 0.508$ mm (Case I in Table 1), where transition is expected to occur as a result of Mack-mode amplification, the measured onset of transition corresponds to $N_{MM} = 7.77$ with an associated disturbance frequency of $F_{MM}(\xi_T) = 1760$ kHz. As the nose-tip bluntness is increased, the Mack-mode waves become progressively less amplified. Configuration II with $R_N = 1.524$ mm and $Re_\infty = 30.5 \times 10^6 \text{ m}^{-1}$ has the same nose Reynolds number, Re_{R_N} , as the baseline case of sharper

Table 1 Details of the AFRL configurations used in the present study, including the measured transition locations (ξ_T) from Ref. [16], the Mack-mode N -factor ($N_{MM}(\xi_T)$) at the transition location, along with the frequency of the most amplified disturbance ($F_{MM}(\xi_T)$). The flow conditions are $M_\infty = 5.9$, $\bar{T}_\infty = 76.74$ K, $\bar{T}_w = 300$ K, and $\bar{T}_w/\bar{T}_{w,ad} = 0.57$.

Case	R_N [mm]	Re_∞ [$\times 10^6$ m $^{-1}$]	Re_{R_N} [$\times 10^3$]	ξ_T [m]	$N_{MM}(\xi_T)$	$F_{MM}(\xi_T)$ [kHz]
I	0.508	91.5	46.48	0.103	7.77	1760
II	1.524	30.5	46.48	0.223	3.75	660
III	1.524	61.0	92.96	0.170	1.14	1000
IV	1.524	91.5	139.4	0.133	0.04	1340
V	2.540	91.5	232.4	0.147	–	–
VI	5.080	91.5	464.8	0.161	–	–
VII	15.24	30.5	464.8	–	–	–
VIII	15.24	61.0	929.6	0.227	–	–
IX	15.24	91.5	1394	0.051	–	–

cone, and yet, the N -factor at the transition location is reduced to $N_{MM}(\xi_T) = 3.75$. The latter N -factor value is deemed too low for transition onset driven by the Mack modes, although the lower disturbance frequency of $F_{MM}(\xi_T) = 660$ kHz corresponding to this N -factor could also account for the reduction in the transition N -factor because of the higher tunnel noise at lower frequencies [7, 14]. The remaining configurations from Table 1 have a larger nose Reynolds number Re_{R_N} and the predicted N -factor at the measured transition location is below 2.0. Therefore, the Mack-mode instability is not expected to be the cause behind the transition onset measured at those conditions. Only a subset of the configurations from Table 1 is selected for the disturbance growth analysis presented in this section. The effect of increasing Reynolds number at a fixed nose-tip radius is studied via cases II, III and IV, while the effect of nose-tip radius for a constant Reynolds number is investigated by considering the cases IV through VI.

Figure 3 shows the effect of the nose-tip radius at a constant Reynolds number of $Re_{\infty,L} = 91.5 \times 10^6$ m $^{-1}$ on the Mach number contours for $R_{N,S} = 1.524$ mm, $R_{N,M} = 2.540$ mm, and $R_{N,L} = 5.080$ mm. The streamwise domain is selected to observe the nose-tip vicinity. The entropy-layer edge, δ_S , is defined as the location where the local entropy increment is 0.25 times the entropy increment at the wall ($\Delta S(\xi, \eta = \delta_S) = 0.25\Delta S_{wall}$). The entropy increment, ΔS , is defined with respect to the freestream value, i.e., $\Delta S = c_p \ln(\bar{T}/\bar{T}_\infty) - R_g \ln(\bar{p}/\bar{p}_\infty)$. The entropy layer becomes progressively thicker as the nose-tip radius is increased from $R_{N,S} = 1.524$ mm (Fig. 3(a)) to $R_{N,L} = 5.080$ mm (Fig. 3(c)). In all three cases, the local Mach number remains below 4.4 inside the edge of the entropy layer.

The evolution of the boundary-layer thickness and entropy-layer thickness are plotted in Fig. 4 for the cases II to VI from Table 1, which are selected for further analysis. Figure 4(a) shows the effect of freestream Reynolds number at a fixed values of the nose-tip radius. An increase in the Reynolds number parameter reduces the boundary-layer thickness, and therefore, the swallowing of the entropy layer within the boundary layer occurs farther downstream. Figure 4(b) illustrates the effect of increasing nose-tip radius at a constant freestream Reynolds number, which mainly results in an increased entropy layer thickness, although a relatively small increase in the boundary-layer thickness is also observed. For the cone with the highest nose bluntness ($R_{N,L} = 5.080$ mm), the entropy layer is clearly not swallowed by the boundary layer within the entire length of the cone.

B. Modal Instability Characteristics

Experimental measurements and theoretical predictions based on the PSE analysis of Jewell et al. [16] have confirmed that case I ($R_N = 0.508$ mm) is the only case from Table 1 wherein laminar-turbulent transition is driven by the modal growth of planar Mack-mode instabilities. For all other cases, the modal growth of planar Mack-mode instabilities up to the measured transition location is either too small (cases II, III, or IV) or those disturbances remain stable ahead of the transition location (cases V to IX). Figure 5 shows the N -factor envelopes for cases II through VI from Table 1. The respective transition locations measured during the experiments are indicated with filled circles. As the Reynolds number is increased for a constant nose-tip radius, Fig. 5(a) shows a small downstream shift in the upstream portions of the envelope curves, whereas the measured transition location indicates the opposite trend. Figure 5(b) shows that, at the fixed freestream Reynolds number of $Re_{\infty,L} = 91.5 \times 10^6$ m $^{-1}$, the second mode amplification becomes increasingly

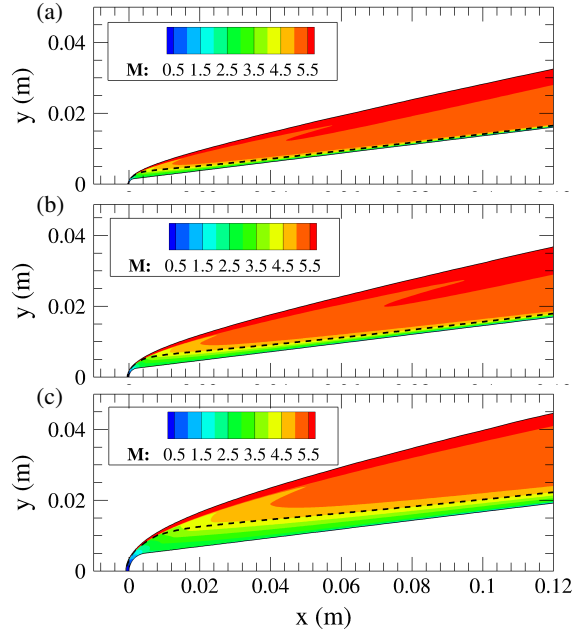


Fig. 3 Mach number (M) contours of the laminar boundary-layer flow over the configurations with $Re_{\infty,L} = 91.5 \times 10^6 \text{ m}^{-1}$ and (a) $R_{N,S} = 1.524 \text{ mm}$, (b) $R_{N,M} = 2.540 \text{ mm}$, and (c) $R_{N,L} = 5.080 \text{ mm}$. The dashed, black line indicates the edge of the entropy layer, δ_S .

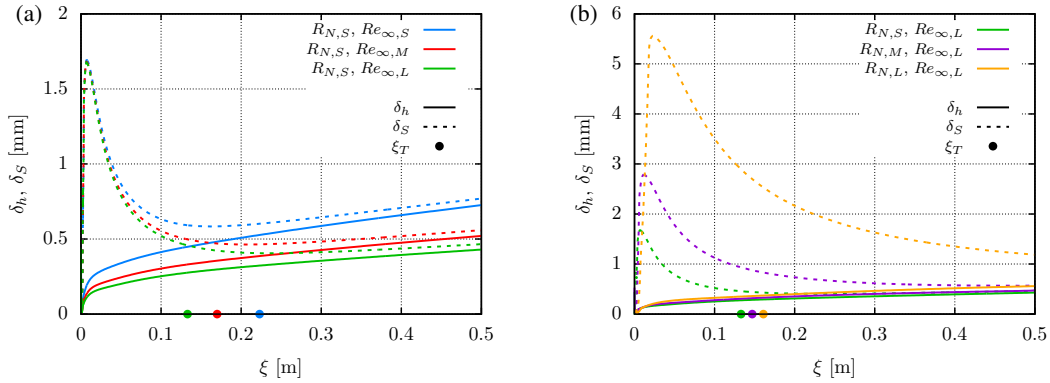


Fig. 4 Streamwise evolution of boundary-layer thickness (δ_h) and entropy-layer thickness (δ_S) of the laminar boundary-layer flows over the configurations with constant (a) nose-tip radius and (b) freestream Reynolds number. The legend refers to $R_{N,S} = 1.524 \text{ mm}$, $R_{N,M} = 2.540 \text{ mm}$, $R_{N,L} = 5.080 \text{ mm}$, $Re_{\infty,S} = 30.5 \times 10^6 \text{ m}^{-1}$, $Re_{\infty,M} = 61.0 \times 10^6 \text{ m}^{-1}$, and $Re_{\infty,L} = 91.5 \times 10^6 \text{ m}^{-1}$. The measured transition locations are indicated with filled circles in the horizontal axis.

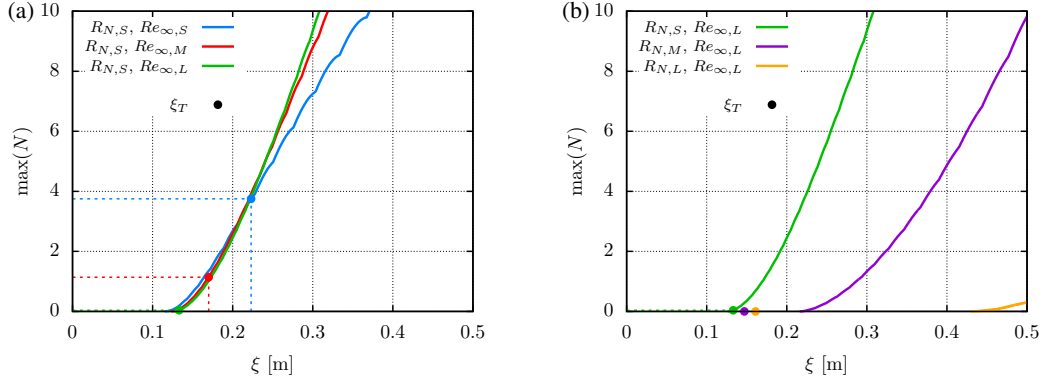


Fig. 5 Streamwise evolution of the N -factor envelope ($\max(N)$) of the laminar boundary-layer flows over the AFRL configurations with constant (a) nose-tip radius and (b) freestream Reynolds number. The legend refers to $R_{N,S} = 1.524$ mm, $R_{N,M} = 2.540$ mm, $R_{N,L} = 5.080$ mm, $Re_{\infty,S} = 30.5 \times 10^6$ m $^{-1}$, $Re_{\infty,M} = 61.0 \times 10^6$ m $^{-1}$, and $Re_{\infty,L} = 91.5 \times 10^6$ m $^{-1}$. The measured transition locations are indicated with filled circles.

weaker at larger values of the nose-tip radius. The location where the second mode begins to be amplified is shifted downstream and, for the case with the largest nose-tip radius ($R_{N,L} = 5.080$ mm), the second mode waves barely begin to get amplified at the end of the cone, resulting in a maximum N -factor of just $\max(N) = 0.3$. The measured transition locations reveal a downward shift in transition with increasing nose bluntness, indicating that transition reversal has not been reached among this subset of cases. Transition reversal is observed for case IX in Table 1, with the measured transition location moving upstream to $\xi_T = 0.051$ m. Despite the absence of transition reversal in Fig. 5(b), the measured onset of transition in all three cases is still associated with a negligible (or even negative) value of the second mode N -factor.

C. Nonmodal Instability Characteristics

For a nonselfsimilar boundary layer such as the boundary layer over blunt cones, both the initial and final locations of the transient growth interval must be varied in order to define the optimal growth characteristics of the flow [23]. A special feature of the transient growth analysis for the blunt cones of interest is that the results naturally split into two parts, one that deals with transient growth intervals that are limited to the nose region, where the results are expected to resemble those for the hemisphere forebody reported by Paredes et al. [23], and a second one that deals with transient growth intervals that extend into the frustum region, where transition usually occurs prior to the onset of transition reversal. Detailed results pertaining to the transient growth of stationary disturbances over the blunt cones of interest were presented earlier by Paredes et al. [3]. Because the stationary disturbances usually yield the highest overall transient growth, their analysis was focused on the zero frequency case. However, motivated by the findings of Cook et al. [4] and Paredes et al. [3], who performed a resolvent analysis of a similar blunt cone configuration at hypersonic conditions and reported appreciable nonmodal growth of planar, traveling waves inside the entropy layer, the transient growth analysis is extended here to traveling disturbances along the frustum region.

Next, we describe the computational predictions for the nonmodal growth of traveling disturbances over the frustum region of the configurations II to VI from Table 1. The selection of these configurations allows for a study of the effects of both the freestream Reynolds number and the nose-tip radius on the nonmodal growth characteristics. Results based on the RHLNSE of Eq. 8 are presented first. The procedure for optimal growth analysis of traveling disturbances based on the RHLNSE is similar to the PSE analysis of stationary disturbances with $\alpha = 0$ by Paredes et al. [3], except for the addition of the streamwise pressure gradient term that is approximated with Eq. (10) based on the work related to PNS equations by Vigneron et al. [32]. For the results presented herein, we confine our attention to transient growth intervals within the frustum of the cone, such that the inflow location lies close to the juncture with the hemispherical nose tip and the outflow location corresponds to the transition location measured by Jewell et al. [16] as indicated in Table 1. The selection of the inflow location was based on a parametric study, which showed that the maximum energy gain occurs for initial locations near the juncture for most combinations of frequency and azimuthal wavenumber, and that the predicted values of the maximum energy amplification were nearly insensitive to further upstream movement of that location.

Figure 6 shows the contours of the N -factor based on the total energy gain, N_E , as a function of the frequency, F ,

and azimuthal wavenumber, m , for the five selected configurations (i.e., cases II to VI from Table 1). The outlet energy gain is selected as the objective function for the optimal growth analysis, based on its success with transition correlation over blunt nosetips [44, 45]. For each configuration in Fig. 6, the maximum energy gain is achieved by a stationary ($F = 0.0$ kHz), three-dimensional perturbation. This stationary disturbance corresponds to the three-dimensional streaks studied by Paredes et al. [3, 5]. Additionally, Figs. 6 shows that the nonmodal growth persists up to progressively higher disturbance frequencies when either the freestream Reynolds number or the nose-tip radius are increased, or equivalently, as the nose Reynolds number (Re_{R_N}) is increased. Also, Fig. 6(c) reveals the emergence of a new peak in the N -factor contours for planar waves ($m = 0$) that are different from the second mode instabilities. As Re_{R_N} is further increased, the energy gain associated with this planar-wave peak becomes larger (Fig. 6(d)) before decreasing again for the largest bluntness configuration in Fig. 6(e). However, the latter case also shows that the energy gain for the planar traveling disturbances is now larger than the gain factors for the neighboring group of three-dimensional traveling disturbances. We note that, in order to focus on the nonmodal growth, the combination of parameters that lead to a predominantly modal growth of second mode waves are blacked out in Figs. 6(a) and 6(b) because of the neglect of the pressure gradient term in the RHLNSE. The modal growth of second mode waves can be captured by using the HLNSE instead.

Next, further details concerning the streamwise evolution of the optimal disturbances are discussed for selected cases. Figure 7 shows the results for planar ($m = 0$) optimal disturbance with $F = 660$ kHz over a streamwise interval corresponding to $(\xi_0, \xi_1) = (0.014, 0.223)$ m, for the $R_{N,S} = 1.514$ mm cone with $Re_{\infty,S} = 30.5 \times 10^6 \text{ m}^{-1}$. The axial growth in the disturbance amplitude in terms of the N -factors based on the total energy (N_E) and kinetic energy (N_K) show a dual peak in disturbance amplification, which is qualitatively similar to the wind tunnel measurements by Marineau et al. [7] on 7° half-angle, blunt cones in Tunnel 9 at Mach 10 and $Re_\infty = 16 \times 10^6 \text{ m}^{-1}$. Specifically, for the 12.7 mm nosetip ($Re_{R_N} = 215.9 \times 10^3$), Marineau et al. [7] reported increasing spectral amplitudes near the nosetip over a wide range of frequencies and a subsequent decrease followed by an eventual increase due to second mode instabilities. The differences in the evolution of N_E and N_K , respectively, up to $\xi \approx 0.18$ m in 7 are attributed to the nonmodal character of the first peak in this disturbance amplification curve. The higher values of N_E indicate the stronger growth of thermodynamic fluctuations during this phase of transient growth. The PSE prediction for the modal growth of the second mode demonstrate that the peak N -factor values achieved by the optimal disturbance initiated close to the nose tip are very similar to those of the modal amplification. The similarity between the dual peak evolution of the disturbance amplitude in the computation (Fig. 7) and the wind tunnel experiment [7] suggests that, at least in certain cases of disturbance evolution over blunt cones, nonmodal growth could occur as a separate precursor to the modal growth in conventional wind tunnels. Of course, the relative magnitude of the nonmodal growth in an actual experiment will depend on the receptivity mechanisms involved. Therefore, it will be useful to investigate the receptivity mechanisms associated with the nonmodal disturbances in addition to those for the modal disturbances. The contours of normalized temperature fluctuation $\tilde{T}/\max(\tilde{T})$ and streamwise velocity $\tilde{u}/\max(\tilde{u})$ in Fig. 7 show that the first N -factor peak involves a combined amplification of temperature fluctuations along the edge of the entropy layer (i.e., outside of the boundary layer) and streamwise velocity fluctuations within the boundary layer. As the disturbance amplitude decreases downstream of the first peak, the second mode becomes dominant, with the peaks of both temperature and streamwise velocity fluctuations occurring inside the boundary layer. As previously explained, the solution obtained with the RHLNSE is not accurate when the second mode is present, which is why the HLNSE were used in this case to calculate the optimal disturbance and its evolution.

Figure 8 shows the results for optimal disturbance growth over a streamwise interval of $(\xi_0, \xi_1) = (0.014, 0.133)$ for the $R_{N,S} = 1.514$ mm cone at a Reynolds number of $Re_{\infty,L} = 91.5 \times 10^6 \text{ m}^{-1}$. Results for three combinations of disturbance frequency and azimuthal wavenumber are shown in this figure. Fig. 8(a) corresponds to an oblique stationary disturbance with $F = 0$ kHz and $m = 80$, 8(b) displays the predictions for the oblique traveling disturbance with $F = 420$ kHz and $m = 80$, whereas 7(c) corresponds to a planar traveling disturbance with $F = 420$ kHz and $m = 0$. The three-dimensional stationary optimal disturbance of Fig. 8(a) corresponds to the optimal streaks that were thoroughly studied by Paredes et al. [3, 5]. The N -factor curves based on the total and kinetic energies of the disturbance show a similar evolution as each other and the temperature and streamwise velocity fluctuations are contained within the boundary-layer thickness. The three-dimensional traveling disturbance from Fig. 8(b) has a notably different structure than the stationary streak of Fig. 8(a). The peak N -factor based on the kinetic energy is lower by $\Delta N \approx 1$ than that based on the total energy, showing a relatively stronger amplification of thermodynamic fluctuations. This effect is even more prominent for the planar traveling disturbance of Fig. 8(c), where the N_K peak is lower than N_E by $\Delta N \approx 2$. The mode shape evolutions for the optimal traveling disturbances of Figs. 8(b) and 8(c) show that the disturbances are initially tilted against the flow direction and increase in magnitude while rotating downstream. This behavior strongly resembles the Orr mechanism for the transient growth of planar disturbances [46, 47], which has been widely studied for

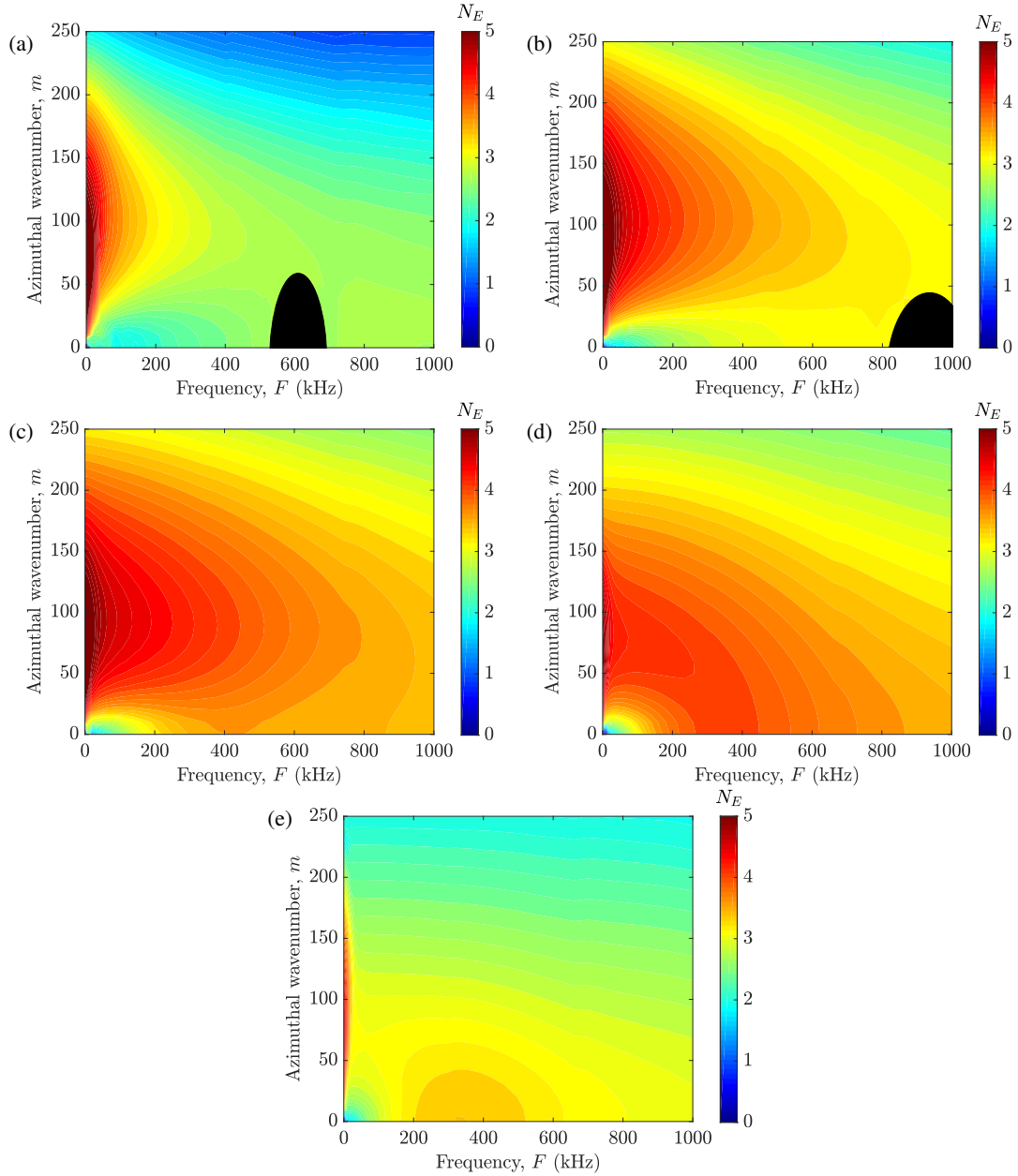


Fig. 6 Contours of N -factor values defined as $N_E = 1/2\ln(G_E^{out})$ and computed with RHLNSE in the azimuthal wavenumber versus frequency plane of laminar boundary-layer flow over the selected configurations from Table 1: (a) II ($R_{N,S} = 1.524$ mm, $Re_{\infty,S} = 30.5 \times 10^6$ m $^{-1}$, $(\xi_0, \xi_1) = (0.014, 0.223)$ m), (b) III ($R_{N,S} = 1.524$ mm, $Re_{\infty,M} = 61.0 \times 10^6$ m $^{-1}$, $(\xi_0, \xi_1) = (0.014, 0.170)$ m), (c) IV ($R_{N,S} = 1.524$ mm, $Re_{\infty,L} = 91.5 \times 10^6$ m $^{-1}$, $(\xi_0, \xi_1) = (0.014, 0.133)$ m), (d) V ($R_{N,M} = 2.540$ mm, $Re_{\infty,L} = 91.5 \times 10^6$ m $^{-1}$, $(\xi_0, \xi_1) = (0.015, 0.147)$ m), and (e) VI ($R_{N,L} = 5.080$ mm, $Re_{\infty,L} = 91.5 \times 10^6$ m $^{-1}$, $(\xi_0, \xi_1) = (0.020, 0.161)$ m). The regions with modal growth of second mode are blacked out.

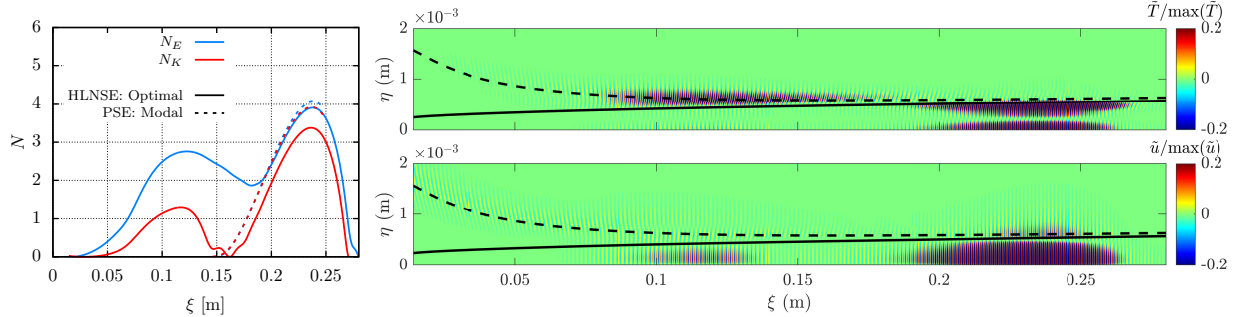


Fig. 7 Evolution of N -factor based on total energy (N_E) and kinetic energy (N_K), and contours of normalized temperature and streamwise velocity components of the optimal disturbance computed by using the HLNSE and with $(F, m) = (660 \text{ kHz}, m = 0)$ and $(\xi_0, \xi_1) = (0.014, 0.223) \text{ m}$, for the $R_{N,S} = 1.514 \text{ mm}$ cone with $Re_{\infty,S} = 30.5 \times 10^6 \text{ m}^{-1}$. The N -factor evolution for the second mode with the same frequency and azimuthal wavenumber computed with PSE is added on the left plot with dashed lines. The solid and dashed black lines indicate the edge of the boundary layer, δ_h , and the edge of the entropy layer, δ_S , respectively.

incompressible flows [48, 49]. Nonmodal growth based on the Orr mechanism is attributed to the extraction of energy from the mean shear by transporting momentum down the mean momentum gradient through the action of the Reynolds stress associated with the perturbation field. However, the energy amplification observed in this compressible case is mainly attributed to the temperature perturbations within the entropy layer, where there exists a gradient in the mean flow temperature. Similar to the LIF-based schlieren images of Grossir et al. [50], the peak disturbance magnitude at any axial location is observed outside of the mean boundary-layer edge (Fig. 2). However, additional work is required to establish a more definitive link between the experimental observations and the nonmodal growth mechanism reported herein. Furthermore, because the traveling mode structures in Fig. 8(b) and 8(c) have no evident or relatively weak, respectively, signature within the boundary-layer region (i.e., below the boundary-layer edge), their role in initiating boundary-layer transition also remains to be clarified. Similarly, nonlinear simulations of these traveling instabilities, e.g., by means of nonlinear PSE or DNS, could provide some insights into the potential breakdown mechanism and also into the minimum initial amplitude of the optimal disturbance that would likely result in the onset of transition at the measured transition location.

Finally, we consider the details of the traveling disturbance amplification for case VI from Table 1 (i.e., $R_{N,L} = 5.080 \text{ mm}$ and $Re_{\infty,L} = 91.5 \times 10^6 \text{ m}^{-1}$), which corresponds to the highest value of the nosetip Reynolds number ($Re_R N = 5.080 \text{ mm}$) considered in this paper. Figure 9 illustrates the evolution of the high frequency disturbance with the largest nonmodal amplification in this case, which now corresponds to a purely axisymmetric wave ($m = 0$) with a frequency of $F = 320 \text{ kHz}$ as shown in the energy gain contours of Fig. 6(e). The evolution of N_E is notably different from that of N_K , with the peak value of N_E at $\xi = 0.185 \text{ m}$ being equal to $\max(N_E) = 3.5$, whereas the peak of N_K is located at $\xi = 0.143 \text{ m}$ and has a considerably smaller value of $\max(N_K) = 1.7$. The mode shape evolution also shows strong differences between the temperature and streamwise velocity components of the disturbance. While the fluctuations in both components are confined below the entropy-layer edge, the streamwise velocity show a double peak structure in wall-normal direction in the vicinity of the N_K peak near $\xi = 0.14 \text{ m}$. Again, we note that the role of this disturbance in initiating boundary-layer transition remains to be seen, especially in view of its weak signature near the wall.

IV. Summary and Concluding Remarks

Optimal transient growth analysis has been conducted for the laminar boundary layer flow over a 7° half-angle, variable nose-bluntness cone at zero angle of attack. Computations are performed for a selected set of nose bluntness and freestream conditions from the measurements by Jewell et al. [16] in the AFRL Mach 6 High Reynolds Number facility. With a cone length of approximately 0.5 meters, the selected test conditions cover a unit Reynolds number range of $Re_\infty = 30.5 - 91.4 \times 10^6 \text{ m}^{-1}$. The present analysis extends the previous work on transient growth of stationary disturbances [3, 5] to the nonmodal growth of both axisymmetric and azimuthally-varying traveling disturbances that are initiated near the nosetip of the cone for several combinations of bluntness and freestream Reynolds number. Consistent with the previous findings for axisymmetric disturbances by Cook et al. [4] and Paredes et al. [5], the present transient growth analysis showed that cone models with sufficiently blunt nose tips can support a significant nonmodal growth of

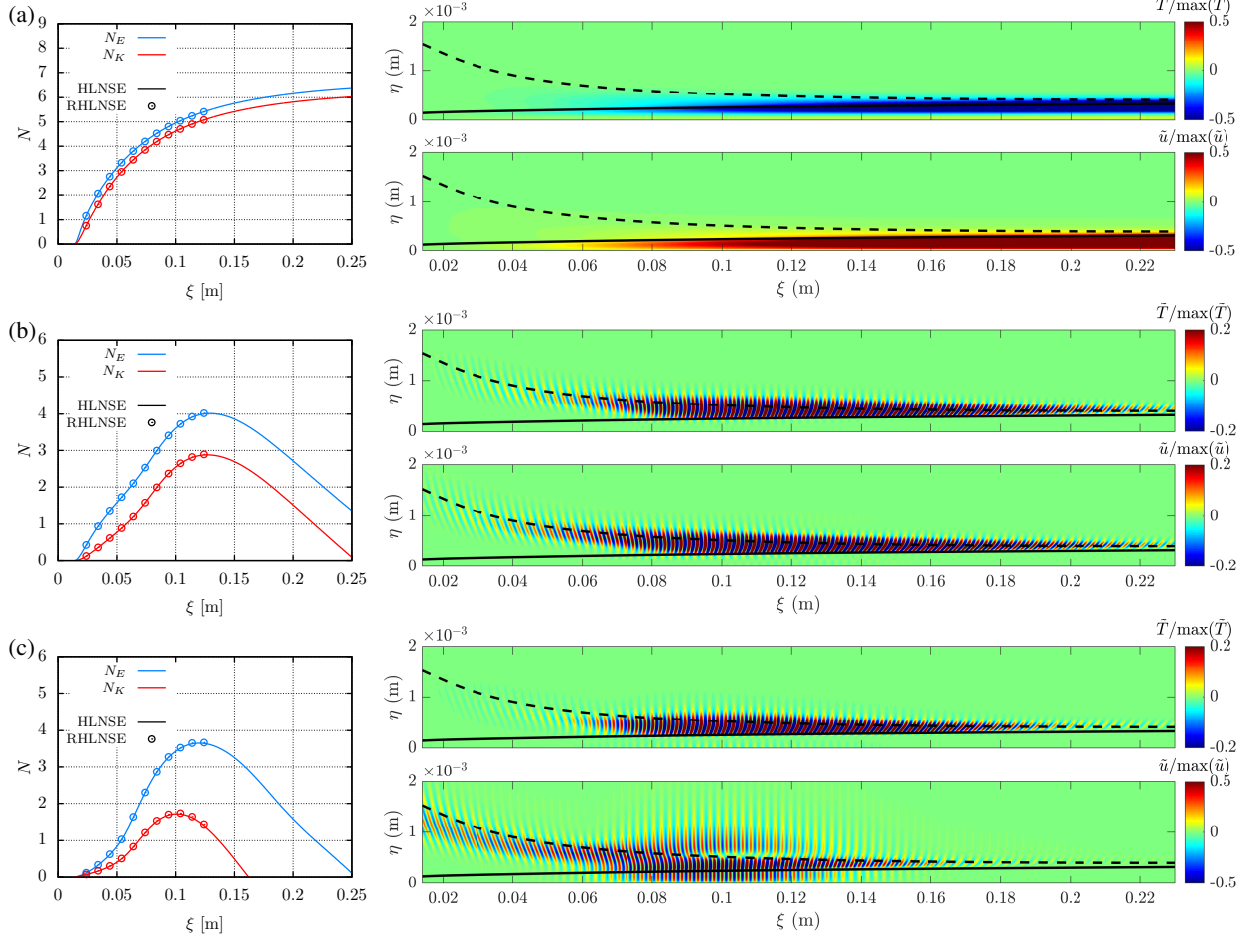


Fig. 8 Evolution of N -factor based on total energy (N_E) and kinetic energy (N_K), and contours of normalized temperature and streamwise velocity components of the optimal disturbance computed with RHLNSE for (a) a stationary disturbance with $(F, m) = (0 \text{ kHz}, m = 80)$, (b) an oblique traveling disturbance with $(F, m) = (420 \text{ kHz}, m = 80)$, and (c) a planar traveling mode with $(F, m) = (420 \text{ kHz}, m = 0)$. The three cases are computed with $(\xi_0, \xi_1) = (0.014, 0.133) \text{ m}$, for the $R_{N,S} = 1.514 \text{ mm}$ cone with $Re_{\infty,L} = 91.5 \times 10^6 \text{ m}^{-1}$. The solid and dashed black lines indicate the edge of the boundary layer, δ_h , and the edge of the entropy layer, δ_S , respectively.

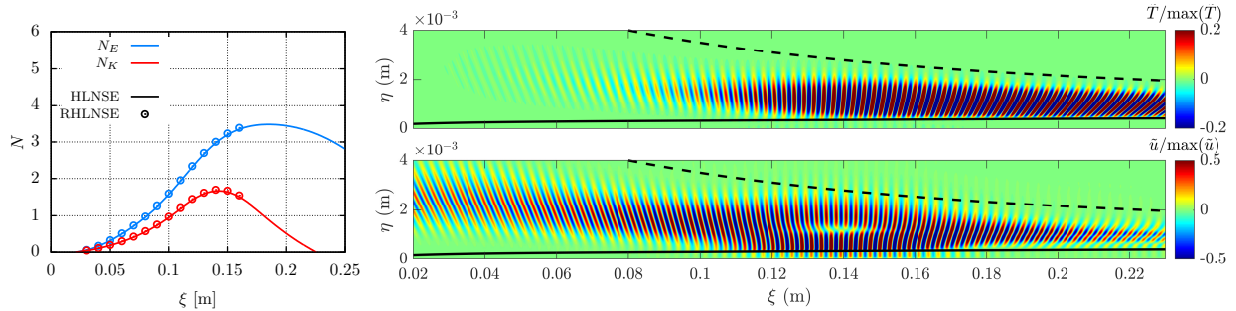


Fig. 9 Evolution of N -factor based on total energy (N_E) and kinetic energy (N_K), and contours of normalized temperature and streamwise velocity components of the optimal disturbance computed by using the RHLNSE and with $(F, m) = (340 \text{ kHz}, m = 0)$ and $(\xi_0, \xi_1) = (0.020, 0.161) \text{ m}$, for the $R_{N,L} = 5.080 \text{ mm}$ cone with $Re_{\infty,L} = 91.5 \times 10^6 \text{ m}^{-1}$. The solid and dashed black lines indicate the edge of the boundary layer, δ_h , and the edge of the entropy layer, δ_S , respectively.

planar waves with peak fluctuations in between the edges of the boundary layer and the entropy layer. This finding may account for the schlieren observations of Grossir et al. [50], which include a visible signature of disturbances outside the boundary layer.

For the small bluntness case studied herein, selected axisymmetric disturbances were shown to exhibit an initial nonmodal disturbance growth as the precursor to the modal growth of second mode waves. The intermediate decay between the regions of nonmodal and modal amplification resulted in a dual peak evolution of the disturbance amplitude. Such dual peak evolution cannot be explained via modal growth alone and has also been observed in the blunt cone measurements of Marineau et al. [7]. As the bluntness parameter is increased further, the modal growth becomes negligible and the optimal energy gain is dominated by nonmodal mechanisms. Computational results in this regime have shown that the frequency spectrum of the energy gain for axisymmetric traveling disturbances displays a peak at a finite frequency even in the absence of (significant) modal amplification. Yet, over an intermediate range of bluntness values, the peak energy gain for axisymmetric disturbances may be less than the energy gain for oblique disturbances of the same frequency. The peak fluctuations associated with the latter, three-dimensional traveling disturbances occur outside the boundary layer region, making these disturbances rather different from the family of predominantly longitudinal streaks that dominates the optimal growth of stationary and low-frequency disturbances. On the other hand, the planar disturbances have a more evident signature within the boundary-layer region, which could make them more visible in surface pressure measurements (such as those performed by Marineau et al. [7]) as well as providing them a potentially stronger role in initiating boundary-layer transition. Both axisymmetric and three-dimensional optimal growth disturbances are initially tilted against the flow direction while they are increasing in amplitude, but their orientation with respect to the surface gradually rotates to the opposite direction. This trend strongly resembles the Orr mechanism for the transient growth of planar disturbances in incompressible flows [48], but the temperature variations are also expected to play a significant part during the energy transfer in the present case. Furthermore, the temperature component of the disturbance is significantly more amplified than the streamwise velocity fluctuation for the axisymmetric traveling disturbances. The computational results also suggest that, for optimal growth over a specified interval of interest, the peak of the energy gain contours in the frequency-azimuthal wavenumber plane migrates to purely axisymmetric disturbances at sufficiently large values of the bluntness parameter.

We note that while the present results may provide a potential explanation for an interesting feature of the measured frequency spectra in the wind tunnel measurements over blunt cones, their scope does not extend to providing a definitive link between the nonmodal growth of disturbances and the observed onset of transition in absence of modal disturbance growth. Performing parallel measurements in both quiet and conventional wind tunnel facilities, or during flight test experiments, would provide further information regarding the role of the freestream disturbances and the nonmodal growth of traveling disturbances within the entropy layer during the transition process.

Acknowledgments

This research was sponsored by the NASA Transformational Tools and Technologies (TTT) Project of the Transformative Aeronautics Concepts Program (TACP) and by the Hypersonic Technology Project (HTP) under the Aeronautics Research Mission Directorate (ARMD). Dr. Joshep S. Jewell was supported by the National Research Council (NRC) Research Associateship for part of this work. Comments on this manuscript by Dr. Heather Kline, Ms. Elizabeth Lee-Rausch, and Dr. Steven Bauer are also gratefully acknowledged.

References

- [1] Schneider, S., "Hypersonic Laminar-Turbulent Transition on Circular Cones and Scramjet Forebodies," *Progress in Aerospace Sciences*, Vol. 40, 2004, pp. 1–50. doi:10.1016/j.paerosci.2003.11.001.
- [2] Stetson, K., "Nosetip Bluntness Effects on Cone Frustum Boundary Layer Transition in Hypersonic Flow," AIAA Paper 83-1763, 1983. doi:10.2514/6.1983-1763.
- [3] Paredes, P., Choudhari, M., Li, F., Jewell, J., Kimmel, R., Marineau, E., and Grossir, G., "Nosetip Bluntness Effects on Transition at Hypersonic Speeds: Experimental and Numerical Analysis Under NATO STO AVT-240," AIAA Paper 2018-0057, 2018. doi:10.2514/6.2018-0057.
- [4] Cook, D., Thome, J., Brock, J., Nichols, J., and Candler, G., "Understanding Effects of Nose-Cone Bluntness on Hypersonic Boundary Layer Transition using Input-Output Analysis," AIAA Paper 2018-0378, 2018. doi:10.2514/6.2018-0378.

- [5] Paredes, P., Choudhari, M., Li, F., Jewell, J., Kimmel, R., Marineau, E., and Grossir, G., “Nosetip Bluntness Effects on Transition at Hypersonic Speeds: Experimental and Numerical Analysis,” *Journal of Spacecraft and Rockets*, 2018. doi:10.2514/1.A34277.
- [6] Aleksandrova, E., Novikova, A., Utyzhnikov, S., and Fedorov, A., “Experimental Study of the Laminar Turbulent Transition on a Blunt Cone,” *Journal of Applied Mechanics and Technical Physics*, Vol. 55, No. 3, 2014, pp. 375–385. doi:10.1134/S0021894414030018.
- [7] Marineau, E., Moraru, C., Lewis, D., Norris, J., Lafferty, J., Wagnild, R., and Smith, J., “Mach 10 Boundary-Layer Transition Experiments on Sharp and Blunted Cones,” AIAA Paper 2014-3108, 2014. doi:10.2514/6.2014-3108.
- [8] Softley, E., Graber, B., and Zempel, R., “Experimental Observation of Transition of the Hypersonic Boundary Layer,” *AIAA Journal*, Vol. 7, No. 2, 1969, pp. 254–263. doi:10.2514/3.5083.
- [9] Softley, E., “Boundary Layer Transition on Hypersonic Blunt, Slender Cones,” AIAA Paper 69-0705, 1969. doi:10.2514/6.1969-705.
- [10] Grossir, G., Pinna, F., Bonucci, G., Regert, T., Rambaut, P., and Chazot, O., “Hypersonic Boundary Layer Transition on a 7 Degree Half-Angle Cone at Mach 10,” AIAA Paper 2014-2774, 2014. doi:10.2514/6.2014-2779.
- [11] Zanchetta, M., “Kinetic Heating and Transition Studies and Hypersonic Speeds,” Ph.D. thesis, Imperial College of Science, Technology and Medicine, London, 1996. URL <https://spiral.imperial.ac.uk/handle/10044/1/37124>.
- [12] Malik, M., Spall, R., and Chang, C.-L., “Effect of Nose Bluntness on Boundary Layer Stability and Transition,” AIAA Paper 90-0112, 1990. doi:10.2514/6.1990-112.
- [13] Herbert, T., and Esfahanian, V., “Stability of Hypersonic Flow over a Blunt Body,” AGARD CP-514. Paper 28. Theoretical and experimental methods in hypersonic flows., 1994.
- [14] Marineau, E., “Prediction Methodology for Second-Mode-Dominated Boundary-Layer Transition in Hypersonic Wind Tunnels,” *AIAA Journal*, Vol. 55, No. 2, 2017, pp. 484–499. doi:10.2514/1.J055061.
- [15] Jewell, J., and Kimmel, R., “Boundary Layer Stability Analysis for Stetson’s Mach 6 Blunt Cone Experiments,” *Journal of Spacecraft and Rockets*, Vol. 54, No. 1, 2017, pp. 258–265. doi:10.2514/1.A33619.
- [16] Jewell, J., Kennedy, R., Laurence, S., and Kimmel, R., “Transition on a Variable Bluntness 7-Degree Cone at High Reynolds Number,” AIAA Paper 2018-1822, 2018. doi:10.2514/6.2018-1822.
- [17] Dietz, G., and Hein, S., “Entropy-Layer Instabilities over a Blunted Flat Plate in Supersonic Flow,” *Physics of Fluids*, Vol. 11, No. 1, 1999, pp. 7–9. doi:10.1063/1.869899.
- [18] Fedorov, A., and Tumin, A., “Evolution of Disturbances in Entropy Layer on Blunted Plate in Supersonic Flow,” *AIAA Journal*, Vol. 42, No. 1, 2004, pp. 89–94. doi:10.2514/1.9033.
- [19] Pralits, J., Airiau, C., Hanifi, A., and Henningson, D., “Sensitivity Analysis using Adjoint Parabolized Stability Equations for Compressible Flows,” *Flow, Turbulence and Combustion*, Vol. 65, 2000, pp. 321–346. doi:10.1023/A:1011434805046.
- [20] Tempelmann, D., Hanifi, A., and Henningson, D., “Spatial Optimal Growth in Three-Dimensional Boundary Layers,” *Journal of Fluid Mechanics*, Vol. 646, 2010, pp. 5–37. doi:10.1017/S0022112009993260.
- [21] Tempelmann, D., Hanifi, A., and Henningson, D., “Spatial Optimal Growth in Three-Dimensional Compressible Boundary Layers,” *Journal of Fluid Mechanics*, Vol. 704, 2012, pp. 251–279. doi:10.1017/jfm.2012.235.
- [22] Paredes, P., Choudhari, M., Li, F., and Chang, C.-L., “Optimal Growth in Hypersonic Boundary Layers,” *AIAA Journal*, Vol. 54, No. 10, 2016, pp. 3050–3061. doi:10.2514/1.J054912.
- [23] Paredes, P., Choudhari, M., and Li, F., “Blunt-Body Paradox and Transient Growth on a Hypersonic Spherical Forebody,” *Physical Review Fluids*, Vol. 2, 2017, p. 053903. doi:10.1103/PhysRevFluids.2.053903.
- [24] Andersson, P., Berggren, M., and Henningson, D., “Optimal Disturbances and Bypass Transition in Boundary Layers,” *Physics of Fluids*, Vol. 11, 1999, pp. 134–150. doi:10.1063/1.869908.
- [25] Luchini, P., “Reynolds-Number-Independent Instability of the Boundary Layer over a Flat Surface: Optimal Perturbations,” *J. Fluid Mech.*, Vol. 404, 2000, pp. 289–309. doi:10.1017/S0022112099007259.

- [26] Tumin, A., and Reshotko, E., "Optimal Disturbances in Compressible Boundary Layers," *AIAA Journal*, Vol. 41, 2003, pp. 2357–2363. doi:10.2514/2.6860.
- [27] Li, F., and Malik, M., "Mathematical Nature of Parabolized Stability Equations," *R. Kobayashi (Ed.), Laminar-Turbulent Transition*, Springer, 1994, pp. 205–212. doi:10.1007/978-3-642-79765-1_24.
- [28] Li, F., and Malik, M., "On the Nature of the PSE Approximation," *Theoretical and Computational Fluid Dynamics*, Vol. 8, No. 4, 1996, pp. 253–273. doi:10.1007/BF00639695.
- [29] Li, F., and Malik, M., "Spectral Analysis of Parabolized Stability Equations," *Computers & Fluids*, Vol. 26, No. 3, 1997, pp. 279–297. doi:10.1016/S0045-7930(96)00044-8.
- [30] Haj-Hariri, H., "Characteristics Analysis of the Parabolized Stability Equations," *Studies Applied Mathematics*, Vol. 92, 1994, pp. 41–53. doi:10.1002/sapm199492141.
- [31] Bagheri, S., and Hanifi, A., "The Stabilizing Effect of Streaks on Tollmien-Schlichting and Oblique Waves: A Parametric Study," *Physics of Fluids*, Vol. 19, 2007, pp. 078103–1–4. doi:10.1063/1.2746047.
- [32] Vigneron, Y., Rakich, J., and Tannehill, J., "Calculation of Supersonic Viscous Flow over Delta Wings With Sharp Supersonic Leading Edges," AIAA Paper 78-1137, 1978. doi:10.2514/6.1978-1137.
- [33] Chang, C., Malik, M., Erlebacher, G., and Hussaini, M., "Compressible Stability of Growing Boundary Layers using Parabolized Stability Equations," AIAA Paper 1991-1636, 1991. doi:10.2514/6.1991-1636.
- [34] Chang, C.-L., "Langley Stability and Transition Analysis Code (LASTRAC) Version 1.2 User Manual," NASA TM-2004-213233, 2004.
- [35] Zuccher, S., Tumin, A., and Reshotko, E., "Parabolic Approach to Optimal Perturbations in Compressible Boundary Layers," *Journal of Fluid Mechanics*, Vol. 556, 2006, pp. 189–216. doi:10.1017/S0022112006009451.
- [36] Chu, B.-T., "On the Energy Transfer to Small Disturbances in Fluid Flow (PART I)," *Acta Mechanica*, Vol. 1, No. 3, 1956, pp. 215–234.
- [37] Mack, L. M., "Boundary Layer Stability Theory," Tech. Rep. Jet Propulsion Laboratory Report 900-277, California Institute of Technology, Pasadena, CA, 1969.
- [38] Hanifi, A., Schmid, P., and Henningson, D., "Transient Growth in Compressible Boundary Layer Flow," *Physics of Fluids*, Vol. 8, 1996, pp. 826–837. doi:10.1063/1.868864.
- [39] Hermanns, M., and Hernández, J., "Stable High-Order Finite-Difference Methods Based on Non-Uniform Grid Point Distributions," *International Journal for Numerical Methods in Fluids*, Vol. 56, 2008, pp. 233–255. doi:10.1002/fld.1510.
- [40] Paredes, P., Hermanns, M., Le Clainche, S., and Theofilis, V., "Order 10^4 Speedup in Global Linear Instability Analysis using Matrix Formation," *Computer Methods in Applied Mechanics and Engineering*, Vol. 253, 2013, pp. 287–304. doi:10.1016/j.cma.2012.09.014.
- [41] Wright, M., Candler, G., and Bose, D., "Data-Parallel Line Relaxation Method for the Navier-Stokes Equations," *AIAA Journal*, Vol. 36, No. 9, 1998, pp. 1603–1609. doi:10.2514/2.586.
- [42] Johnson, H., "Thermochemical Interactions in Hypersonic Boundary Layer Stability," Ph.D. thesis, University of Minnesota, 2000.
- [43] Johnson, H., Seipp, T., and Candler, G., "Numerical Study of Hypersonic Reacting Boundary Layer Transition on Cones," *Physics of Fluids*, Vol. 10, No. 10, 1998, pp. 2676–2685. doi:10.1063/1.869781.
- [44] Reshotko, E., and Tumin, A., "Role of Transient Growth in Roughness-Induced Transition," *AIAA Journal*, Vol. 42, No. 4, 2004, pp. 766–770. doi:10.2514/1.9558.
- [45] Paredes, P., Choudhari, M., and Li, F., "Blunt-Body Paradox and Improved Application of Transient-Growth Framework," *AIAA Journal*, Vol. 56, No. 7, 2018. doi:10.2514/1.J056678.
- [46] Orr, W., "The Stability Or Instability of the Steady Motions of a Perfect Liquid and of a Viscous Liquid. Part I: A Perfect Liquid," *Proceedings of the Royal Irish Academy A*, Vol. 27, 1907, pp. 9–68. URL <http://www.jstor.org/stable/20490590>.

- [47] Orr, W., “The Stability Or Instability of the Steady Motions of a Perfect Liquid and of a Viscous Liquid. Part II: A Viscous Liquid,” *Proceedings of the Royal Irish Academy A*, Vol. 27, 1907, pp. 69–138. URL <http://www.jstor.org/stable/20490591>.
- [48] Butler, K., and Farrell, B., “Three-Dimensional Optimal Perturbations in Viscous Shear Flow,” *Physics of Fluids*, Vol. 4, No. 8, 1992, pp. 1637–1650. doi:10.1063/1.858386.
- [49] Schmid, P., “Nonmodal Stability Theory,” *Annual Review of Fluid Mechanics*, Vol. 39, 2007, pp. 129–162. doi:10.1146/annurev.fluid.38.050304.092139.
- [50] Grossir, G., Musutti, D., and Chazot, O., “Flow Characterization and Boundary Layer Transition Studies in VKI Hypersonic Facilities,” AIAA Paper 2015-0578, 2015. doi:10.2514/6.2015-0578.